


Article

Mineralogical Characterization of Manganese Oxide Minerals of the Devonian Xialei Manganese Deposit

Sida Niu ^{1,2} , Liqun Zhao ^{1,2,*}, Xiaoju Lin ³, Tong Chen ^{1,2}, Yingchao Wang ^{1,2}, Lingchao Mo ^{1,2}, Xianglong Niu ^{1,2}, Huaying Wu ^{1,2}, Min Zhang ^{1,2}, Jan Marten Huizenga ^{4,5,6} and Peng Long ⁷

- ¹ Institute of Mineral Resources Research, China Metallurgical Geology Bureau, Beijing 101300, China; niusida@cmgb.cn (S.N.); chentong@cmgb.cn (T.C.); wangyingchao@cmgb.cn (Y.W.); molingchao@cmgb.cn (L.M.); niuxianglong@cmgb.cn (X.N.); wuhuaying@cmgb.cn (H.W.); zhangmin@cmgb.cn (M.Z.)
 - ² Mineral Comprehensive Utilization Research and Development Center, China Metallurgical Geology Bureau, Beijing 101300, China
 - ³ Guangdong Provincial Key Laboratory of Mineral Physics and Materials, Guangzhou 510640, China; linxiaoju@gig.ac.cn
 - ⁴ Faculty of Environmental Sciences and Natural Resource Management, Norwegian University of Life Sciences, P.O. Box 5003, NO-1432 Ås, Norway; jan.marten.huizenga@nmbu.no
 - ⁵ Economic Geology Research Institute (EGRU), College of Science and Engineering, James Cook University, Townsville, QLD 4811, Australia
 - ⁶ Department of Geology, University of Johannesburg, P.O. Box 524, Auckland Park, Johannesburg 2006, South Africa
 - ⁷ China Metallurgical Geology Bureau of Geological Prospecting Institute of Guangxi, Nanning 530022, China; longpeng@cmgb.cn
- * Correspondence: zhaoliqun@cmgb.cn



check for updates

Citation: Niu, S.; Zhao, L.; Lin, X.; Chen, T.; Wang, Y.; Mo, L.; Niu, X.; Wu, H.; Zhang, M.; Huizenga, J.M.; et al. Mineralogical Characterization of Manganese Oxide Minerals of the Devonian Xialei Manganese Deposit. *Minerals* **2021**, *11*, 1243. <https://doi.org/10.3390/min11111243>

Academic Editor: Maria Boni

Received: 8 October 2021

Accepted: 5 November 2021

Published: 9 November 2021

Publisher's Note: MDPI stays neutral with regard to jurisdictional claims in published maps and institutional affiliations.



Copyright: © 2021 by the authors. Licensee MDPI, Basel, Switzerland. This article is an open access article distributed under the terms and conditions of the Creative Commons Attribution (CC BY) license (<https://creativecommons.org/licenses/by/4.0/>).

Abstract: The Guangxi Zhuang Autonomous Region is an important manganese ore district in Southwest China, with manganese ore resource reserves accounting for 23% of the total manganese ore resource reserves in China. The Xialei manganese deposit (Daxin County, Guangxi) is the first super-large manganese deposit discovered in China. The Mn oxide in the supergene oxidation zone of the Xialei deposit was characterized using scanning electron microscopy (SEM), energy spectrometer (EDS), transmission electron microscopy (TEM, HRTEM), and X-ray diffraction analysis (XRD). The Mn oxides have a gray-black/steel-gray color, a semi-metallic-earthy luster, and appear as oolitic, pisolitic, banded, massive, and cellular textures. Scanning electron microscopy images show that the manganese oxide minerals are present as fine-spherical particles with an earthy surface. TEM and HRTEM indicate the presence of oriented bundled and staggered nanorods, and nanopores between the crystals. The Mn oxide ore can be classified into two textural types: (1) oolitic and pisolitic (often with annuli) Mn oxide, and (2) massive Mn oxide. Pyrolusite, cryptomelane, and hollandite are the main Mn oxide minerals. The potassium contents of cryptomelane and pyrolusite are discussed. The unit cell parameters of pyrolusite are refined.

Keywords: manganese oxide; Xialei Mn deposit; mineral composition; crystal structure; pyrolusite

1. Introduction

Manganese (Mn) ranks 10th in abundance among the crustal elements. Its valence electron configuration of $3d^54s^2$ with seven valence electrons allows a variable valence (0, +II, +III, +IV, +VI, +VII) [1,2]. Mn occurs in three oxidation states (+II, +III, +IV) in minerals, resulting in a wide variety (more than 30) of Mn oxide and hydroxide minerals. The MnO_6 octahedral structure, which is the basic building block for most Mn oxide minerals, can share edges, corners, or faces to form tunnel and layer structures [2,3].

Manganese oxides are widely distributed in nature and affect the concentration, migration, and bioavailability of heavy metals, organic matter, and nutrient elements in

soil, water, and sediments [4,5]. Lu et al. [6–8] studied the mineral composition and fine structure characteristics of the Fe-Mn oxide “mineral membrane”, which develops on the soil/rock surface when exposed to sunlight. They found evidence for non-classical photosynthesis, indicating that natural Mn oxide plays an important role in biogeochemical interactions between the lithosphere, hydrosphere, and atmosphere.

Natural Mn oxide is low in price and can be used as a source material for Li-Mn batteries. Lithium-manganese oxide batteries have, therefore, a strong price advantage and show great potential because of their excellent power and discharge rate under variable temperature conditions and high voltage frequency [9]. Natural Mn oxides also have good surface adsorption properties and are chemically active. Under different conditions, they can show different degrees of adsorption of heavy metal ions and adsorption and oxidation of anions including NO_3^- , PO_4^{3-} , F^- , and S^{2-} . Manganese oxide can adsorb, transform, and degrade organic pollutants including phenol, ethane, ethylene, and synthetic organic acids, and it can decompose and transform CO_2 , NO_x , and SO_2 [10,11]. All in all, Mn oxides show great potential for the transition to a green economy and mitigating environmental pollution.

The Guangxi Zhuang Autonomous Region is one of the most important Mn ore districts in China. The Mn ore resource reserves account for 23% of the national Mn ore resource reserves in China. The Xialei deposit is the earliest super-large Mn deposit discovered in China with an average grade of Mn oxide ore of ~30% [12,13]. Previous research on the Mn oxide minerals in the Xialei deposit [11,14] has been limited to cryptomelane, i.e., other Mn oxide minerals have not been investigated in detail. Systematic understanding of the Mn oxide minerals in the supergene zone is also in lack for the Mn deposits in China. As a typical example of a super-large manganese deposit in China, the Xialei Mn deposit can be taken as a representative example to investigate the manganese oxide minerals.

Natural Mn oxides that occur in the supergene zone can be present as fine-scale intergrowths of two or more phases that readily alter from one to another, which makes the identification of multiple disordered phases challenging [15]. A combination of different analytical techniques was used, including scanning electron microscopy (SEM), energy spectrometry (EDS), transmission electron microscopy (TEM, HRTEM), Electron Probe Micro Analysis (EPMA), and X-ray diffraction analysis (XRD) to chemically and structurally characterise the Mn oxide minerals in the supergene zone of the Xialei Mn deposit, with the aim to provide a mineral characterisation reference framework of Mn oxide minerals of one of the largest Mn deposits in China.

2. Geological Settings

Situated in the Daxin County (Guangxi), the Xialei Mn deposit is the first super-large Mn deposit discovered in China. The Mn ore resource reserves of Guangxi account for 23% of the total Mn ore resource reserves in China. The study area is located in the Caledonian fold belt in South China (Figure 1a) comprising Cambrian, Devonian-Triassic, Tertiary, and Quaternary strata (Figure 1b).

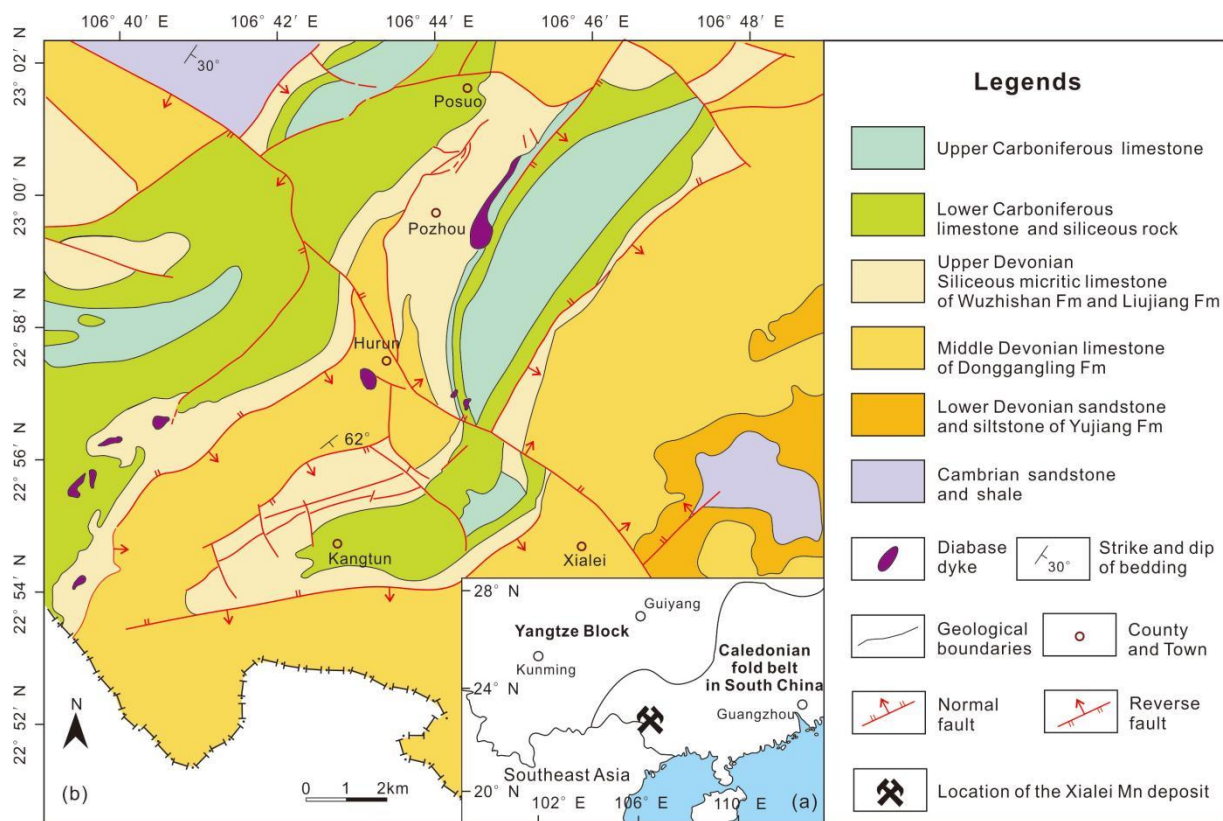


Figure 1. (a) Location and regional geological setting of the Xialei Mn Deposit (modified after [16]); (b) detailed geological map of the Xialei Mn deposit (modified after [17]).

The Xialei Mn deposit is hosted in Devonian and Carboniferous strata with primary Mn carbonate occurring in the Upper Devonian Wuzhishan Formation and the Mn oxide occurring in the supergene oxide zone. The Wuzhishan Formation is divided into three layers, and the stratabound Mn ore body occurs in the middle layer (Figure 2). The upper layer (8–124 m thick) of the Wuzhishan Formation is composed of calcareous limestone, siliceous calcareous mudstone, marlstone, and carbon-bearing siliceous rock and marlstone. The middle layer (10–100 m thick) contains thin layers of siliceous limestone, siliceous rock, Mn carbonate ore bodies, siliceous mudstone intercalated with Mn carbonate, and calcareous mudstone. The lower layer (9–88 m thick) is composed of argillaceous limestone, calcareous mudstone, and lenticle-loaded limestone. The average Mn content of the primary ore is 18–20%, and the average Mn content in the oxidized ore is 28–35% [12]. Minor mafic intrusions including diabase stocks and dykes are present in the region [17].

The Mn ore body is situated in the north-north-east extension of the Shangying syncline. The Upper and Lower Carboniferous limestone occur in the centre of the syncline and are characterized by steep karst mountains with a height of about 400 m. The Upper Devonian siliceous rocks on both limbs of the syncline appear as hills. The Mn oxide ore bodies occur near the surface on the two limbs of the Shangying syncline. Intense folding and faulting of the southern and southwestern limb inverted the stratigraphy, causing the oxidation zone to be deeper (oblique depth of the Mn oxide ore body reaching approximately 50–150 m) than in the northwest limb (oblique depth of the Mn oxide ore body reaching approximately 15 m, [18]). The (quasi) layered Mn oxide ore body follows the folded Mn-bearing Devonian Wuzhishan Formation and retains the appearance of the original stratabound Mn carbonate ore body.

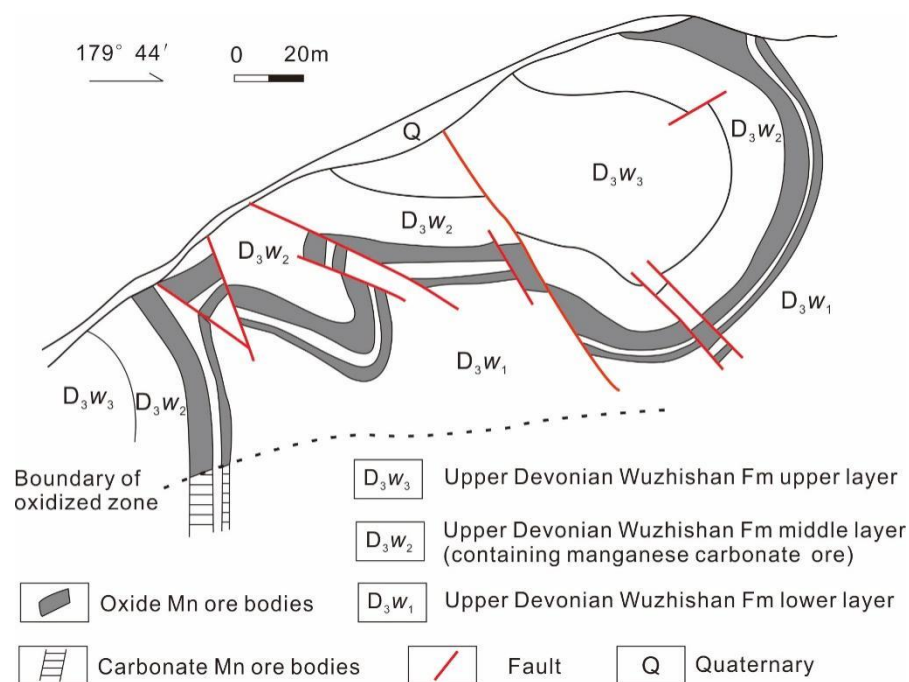


Figure 2. Cross section showing the geometry of supergene Mn oxide bodies (modified after [18]).

3. Methodology

3.1. Sampling and Preparation

The Mn oxide ore from the oxidation zone of the Xialei Mn deposit occurs as black to steel-gray/ brownish red, semi-metallic earthy luster, cryptocrystalline–microcrystalline texture. The Mn oxides are characterized by oolitic and pisolitic (Figure 3a,b), oolitic-banded (Figure 3c), massive-earthy (Figure 3d), massive (Figure 3e), and massive-cellular (Figure 3f) textures.

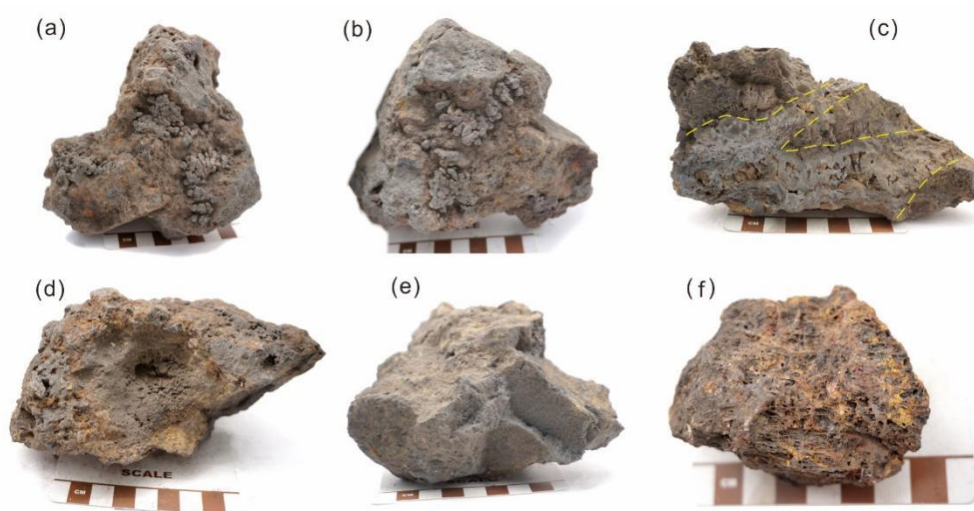


Figure 3. Representative hand specimens of the Mn-oxide ore in the Xialei deposit. (a) and (b) Oolitic and pisolitic texture; (c) oolitic-banded texture (yellow dashed line indicates the banded texture); (d) massive-earthy texture; (e) massive texture; (f) massive-cellular texture.

Two Mn oxide samples (XLO-1 and XLO-2) were collected from the supergene zone in the Xialei Mn deposit. The average Mn mass fraction of XLO-1 (34.2 wt.%) and XLO-2 (34.6 wt.%) was determined using a Thermo Scientific Niton XL 3t XRF analyzer (Table 1). Polished thin sections and polished blocks were prepared for ore microscopy and petrogra-

phy. Mn oxide samples for XRD, SEM, and TEM are Mn oxide minerals selected by gravity separator, selected by binocular microscope and then meshed to power < 200 mesh.

Table 1. Chemical composition of the two Mn oxide samples (XLO-1, XLO-2) from the Xialei deposit by X-Ray Fluorescence (in wt.%).

Sample No.	Mn	Mn Error	Ti	Ti Error	Fe	Fe Error	K	K Error	Ba	Ba Error
XLO-1	20.4	0.855	0.1	0.019	6.1	0.283	1.1	0.213	0.0	0.012
	41.0	1.914	0.2	0.025	10.2	0.521	1.1	0.236	0.7	0.063
	41.3	1.717	0.1	0.021	9.2	0.419	0.9	0.220	0.3	0.031
	30.4	1.461	0.1	0.019	15.2	0.770	0.4	0.191	0.1	0.022
XLO-2	30.8	1.418	0.1	0.019	17.8	0.872	0.4	0.185	0.0	0.016
	42.5	2.579	0.1	0.020	2.5	0.228	0.3	0.198	0.1	0.025
	XLO-1 average	34.2	1.495	0.2	0.022	8.5	0.408	1.1	0.223	0.3
XLO-2 average	34.6	1.819	0.1	0.019	11.8	0.623	0.4	0.191	0.1	0.021

3.2. Experimental Methods

Scanning electron microscopy (SEM) and energy dispersive spectroscopy (EDS). Mn oxide mineral powders (<200 mesh) were pasted onto conductive adhesive for SEM and EDS analysis. SEM observations were carried out on a Hitachi S-3500N scanning electron microscope operated at 24.96 kV. EDS analysis was carried out using an INCA-300 Oxford Instrument. The SEM and EDS analyses were performed at the Beijing General Research Institute of Mining and Metallurgy Technology Group.

Transmission electron microscopy (TEM) and high-resolution transmission electron microscopy (HRTEM). The Mn oxide mineral powder < 200 mesh was embedded with G1 glue for the preparation of ultra-thin sections for TEM and HRTEM analysis. The TEM and HRTEM analyses were carried out at the Beijing General Research Institute of Mining and Metallurgy Technology Group using a JEOL JEM2100 high-resolution transmission electron microscope. An accelerating voltage of 200 kV was used.

X-ray diffraction (XRD). Manganese oxide mineral powder (<200 mesh) was used for XRD analysis, which was carried out at the China University of Geosciences Beijing using a Bruker D2 Phaser X-ray diffractometer with a Cu K α radiation source. X-ray diffraction patterns were collected between 5 and 80° (2 θ) at a scanning rate of 1° (2 θ) min⁻¹ (λ = 0.154 nm, 30 kV, 10 mA). For XRD indexing, the Le Bail routine (Peakfit) and manually picked peaks were combined. The Rietveld method with extraction of the structure factors (Fobs) was then used for refining the unit cell parameters.

Electron probe micro-analysis (EPMA). Major and minor element chemical analysis of the Mn oxides were carried out at the Chinese Academy of Geological Sciences using a JXA-iHP200F Hyper Probe electron microprobe with a 15 kV accelerating voltage, a beam current of 20 nA, a counting time of 10 s (peak position), and a beam diameter of 5 μ m. Standard substances refer to GB/T 15074-2008 general rules for EPMA analysis.

4. Results

4.1. Optical Microscopy

Cryptomelane shows a light whitish green to off-white reflection color with significant pleochroism. The cryptomelane shows an oolitic-pisolitic and massive texture (Figure 4a,b,e). Massive pyrolusite shows earthy-yellow, yellow-white to cream-yellow reflection light, and strong pleochroism. Pyrolusite sometimes occurs as prismatic microcrystals (Figure 4c–e,h). Cracks that resulted from dehydration can be observed (Figure 4f,g). Hollandite shows a yellow-grey reflection color, weak pleochroism, and a colloidal texture (Figure 4g,h). The pyrolusite-cryptomelane-hollandite assemblage occurs, which can be observed under the microscope and in BSE images (Figure 4e,g,h).

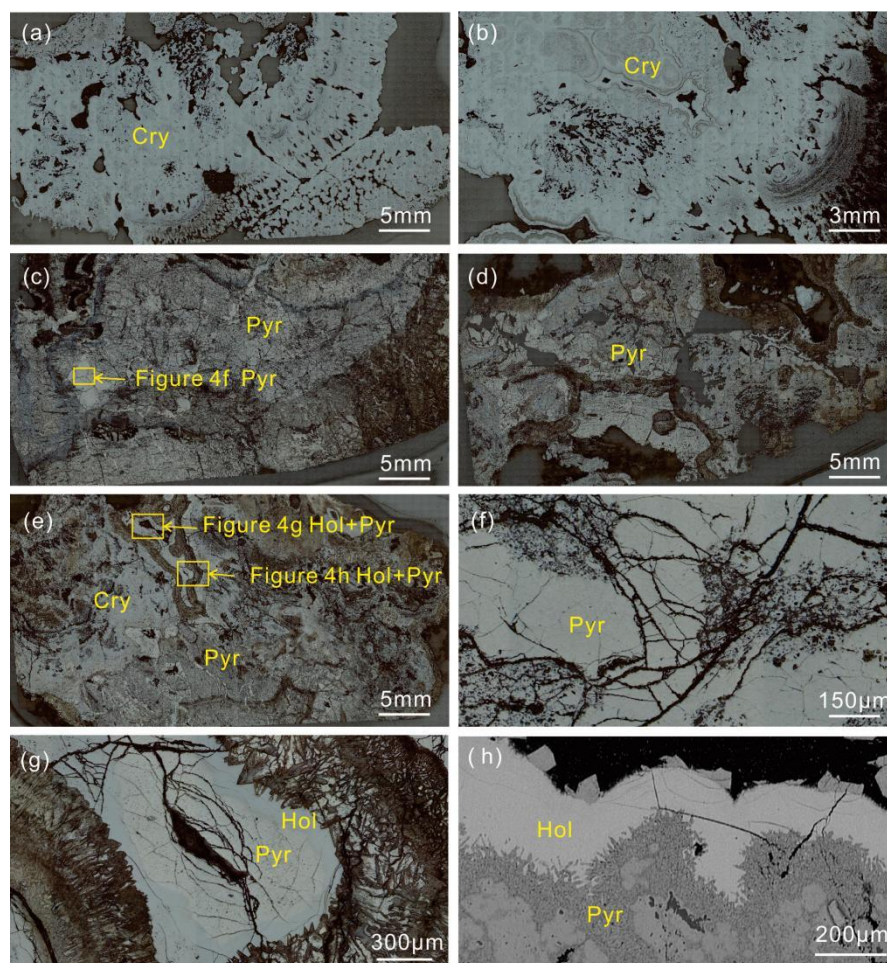


Figure 4. Representative thin section photomicrographs and back-scattered electron images of the Mn-oxide ore in the Xialei deposit. (a,b) Cryptomelane showing light whitish green to off-white reflection color, annulus texture; (c–f) Pyrolusite showing an earthy-yellow, yellow-white to cream-yellow reflection color and a massive texture; (e) Mineral assemblage of pyrolusite, cryptomelane, and hollandite; (g,h) Annule-type texture of pyrolusite and hollandite, with hollandite colloidal structure. Microphotographs (a–g) are reflective light images, the image in (h) is a back-scattered electron image. Cry—Cryptomelane; Pyr—Pyrolusite; Hol—Hollandite.

4.2. SEM and TEM

Scanning electron microscopy images show that the Mn oxide mineral samples in Xialei deposit present as fine-spherical with earthy surface (Figure 5a,b). Tiny loose particles can be observed at 10,000 and 2000 \times magnifications (Figure 5c–f). The EDS results of Mn oxide are shown in Figure 5g,h. Figure 6 presents the TEM and HRTEM images of the tunnels of Mn oxide. Three-dimensional nanorods can be observed with widths and lengths of 5–10 and 200–500 nm, respectively (Figure 6a). The TEM and HRTEM images show the detailed structure of the extended nanorod in the Mn oxide in the Xialei deposit (Figure 6b–e). Nanopores between the crystal grains can be observed with the diameter of the pores ranges from a few to about 60 nm (Figure 6a–e). The fringe distances separated by 0.24 and 0.31 nm with a cross angle of 90 $^\circ$ are in good agreement with the lattice spacings of the (101) and (110) planes of pyrolusite (K_2O wt.% < 1, Ba was not detected by EDS), respectively (Figure 6f). The lattice plane distances are also in agreement with those determined by XRD.

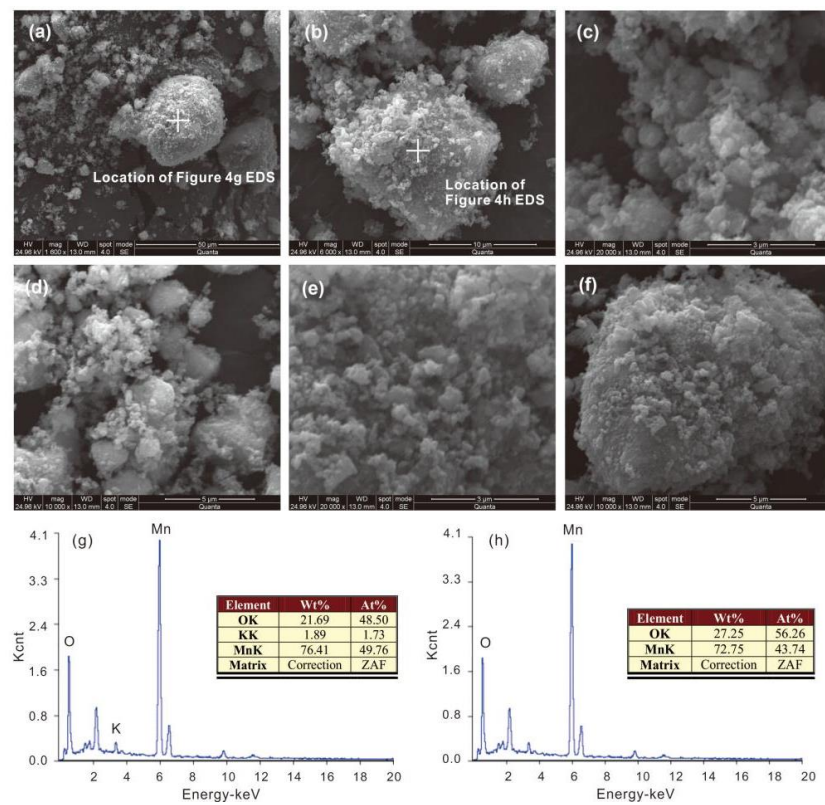


Figure 5. SEM images and EDS results of Mn-oxide powder in the Xialei deposit. (a–f) are SEM images; (g,h) are the EDS results (analyzed points shown in (a,b) correspondingly).

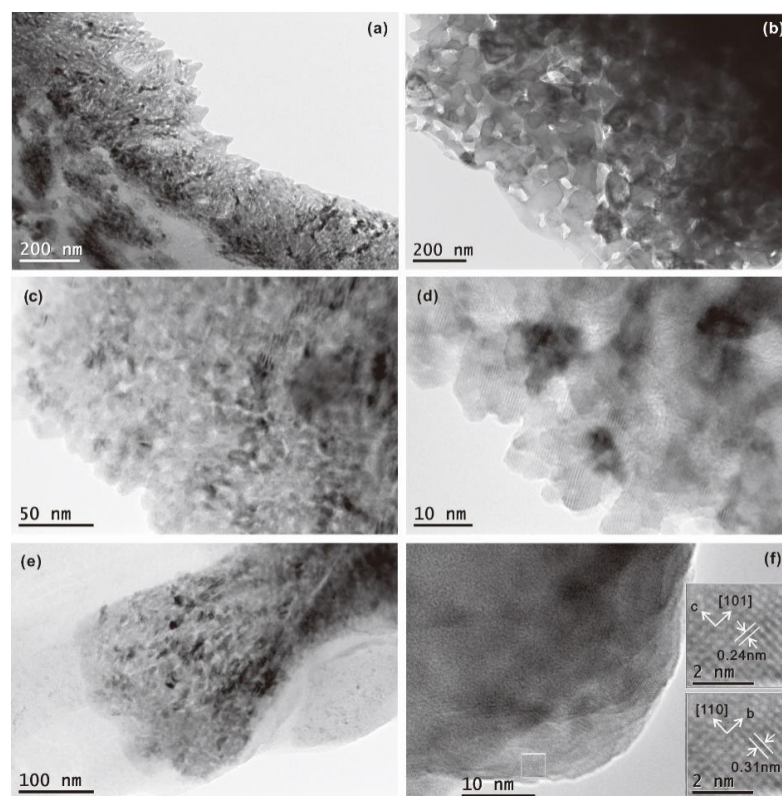


Figure 6. TEM and HRTEM images of Mn oxide ore in the Xialei deposit. (a–d): Pyrolusite in sample XLO-2. (e,f): Pyrolusite in sample XLO-1. (f) Two-dimensional Fourier-filtered lattice image.

4.3. EPMA

The analyzed points for EPMA came from six polished thin sections. Two representative textural types of samples (oolitic and massive) were involved for the EPMA analyses, with 79 points in total (shown in Table S1). The mineral species include cryptomelane, pyrolusite and hollandite. The Mn oxide minerals are composed of MnO (69.87–83.27 wt.%, average value of 77.96 wt.%), K₂O (0.03–4.33 wt.%, average value of 2.01 wt.%), CaO (0.08–1.76 wt.%, average value of 0.65 wt.%), and BaO (0–8.76 wt.%, average value of 0.30 wt.%). Other elements include SiO₂ (<6.96 wt.%, average value of 0.25 wt.%), MgO (<1.98 wt.%, average value of 0.22 wt.%), P₂O₅ (<0.72 wt.%, average value of 0.20 wt.%), Al₂O₃ (0.02–0.66 wt.%, average value of 0.18 wt.%), FeO (<0.19 wt.%, average value of 0.07 wt.%), Na₂O (<0.31 wt.%, average value of 0.06 wt.%), TiO₂ (<0.12 wt.%, average value of 0.02 wt.%), Cr₂O₃ (<0.09 wt.%, average value of 0.02 wt.%), NiO (<0.17 wt.%, average value of 0.02 wt.%), CuO (<0.11 wt.%, average value of 0.02 wt.%), ZrO₂ (<0.08 wt.%, average value of 0.01 wt.%), and PbO (<0.07 wt.%, average value of 0.01 wt.%). The K₂O mass fraction in oolitic and pisolitic structure ranges from 2.31 to 4.33 wt.% (average value of 3.60 wt.%), whereas the K₂O mass fraction in the massive structure ranges between 0.03 and 2.21 wt.% (average value of 0.54 wt.%) (Figure 7). The compositional data and the calculated a.p.f.u. (atoms per formula unit) of the different mineral species are shown in Table S1.

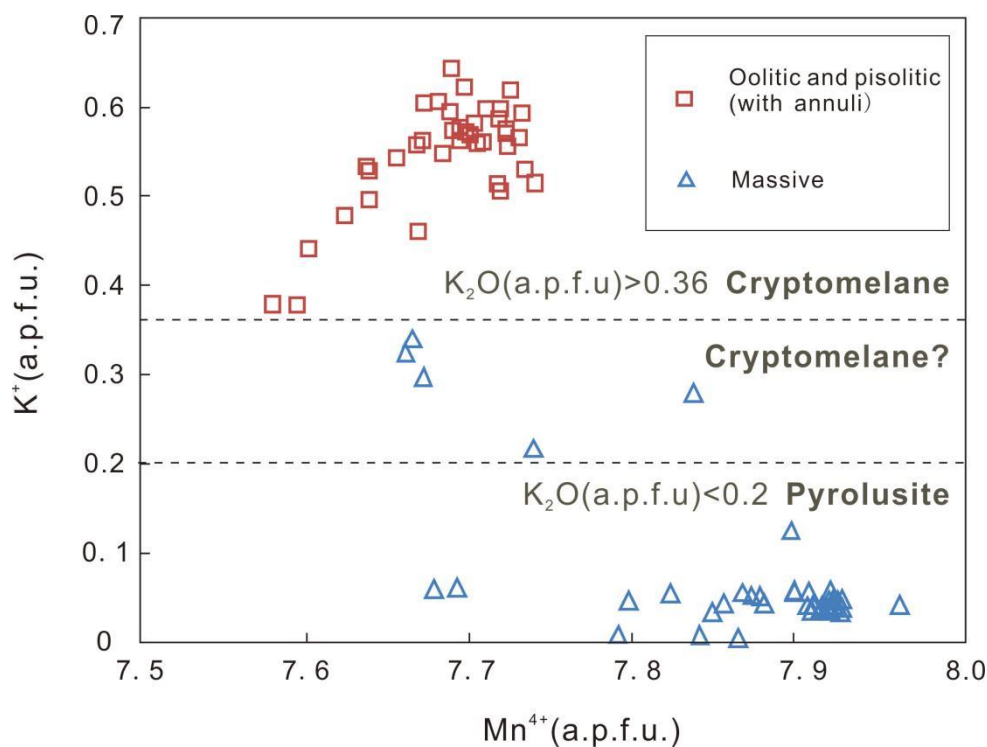


Figure 7. Mn⁴⁺ vs. K⁺ for cryptomelane and pyrolusite.

4.4. XRD

The three strongest XRD peaks for Mn oxide sample XLO-1 are: $2\theta = 28.580^\circ$ ($d = 3.1207 \text{ \AA}$, height = 2565), $2\theta = 37.368^\circ$ ($d = 2.4045 \text{ \AA}$, height = 1850), $2\theta = 56.569^\circ$ ($d = 1.6256 \text{ \AA}$, height = 771), and for Mn oxide sample XLO-2: $2\theta = 26.630^\circ$ ($d = 3.3447 \text{ \AA}$, height = 1808), $2\theta = 28.579^\circ$ ($d = 3.1208 \text{ \AA}$, height = 769), $2\theta = 37.323^\circ$ ($d = 2.4073 \text{ \AA}$, height = 475), $2\theta = 56.605^\circ$ ($d = 1.6246 \text{ \AA}$, height = 360) (all detected peaks are shown in Table 2). A comprehensive analysis (using XRD pattern processing software JADE and Search-Match) combined with the EDS results shows that the Mn oxide samples comprise pyrolusite (PDF No. 72-1984), cryptomelane (PDF No. 44-1386), hollandite (PDF No. 75-1184), and quartz (PDF No. 46-1045) (Figure 8). The pyrolusite unit cell parameters (tetragonal

system, space group $P 42/m n m$) were refined using the Rietveld method returning the following unit cell parameters, i.e., for sample XLO-1: $a = 4.41 (\pm 0.01) \text{ \AA}$, $b = 4.41 (\pm 0.01) \text{ \AA}$, $c = 2.87 (\pm 0.01) \text{ \AA}$, $V = 55.96 (\pm 0.11) \text{ \AA}^3$, and for sample XLO-2: $a = 4.42 (\pm 0.01) \text{ \AA}$, $b = 4.42 (\pm 0.01) \text{ \AA}$, $c = 2.87 (\pm 0.01) \text{ \AA}$, $V = 56.01 (\pm 0.06) \text{ \AA}^3$.

Table 2. XRD peak lists of the Mn oxide in the Xiaiei deposit.

2-Theta	D-Spacing	Intensity	Width
Sample XLO-1			
12.669	6.9816	692	0.233
17.935	4.9416	293	0.332
28.580	3.1207	2565	0.226
37.368	2.4045	1850	0.237
56.569	1.6256	771	0.264
72.419	1.3039	227	0.268
75.663	1.2559	101	0.189
Sample XLO-2			
12.339	7.1672	142	0.089
18.692	4.7432	137	0.094
26.630	3.3447	1808	0.068
28.579	3.1208	769	0.113
37.323	2.4073	475	0.112
42.759	2.1130	206	0.094
56.605	1.6246	360	0.119
59.957	1.5416	351	0.078
67.747	1.3820	215	0.078
68.142	1.3749	259	0.075
72.360	1.3048	151	0.127

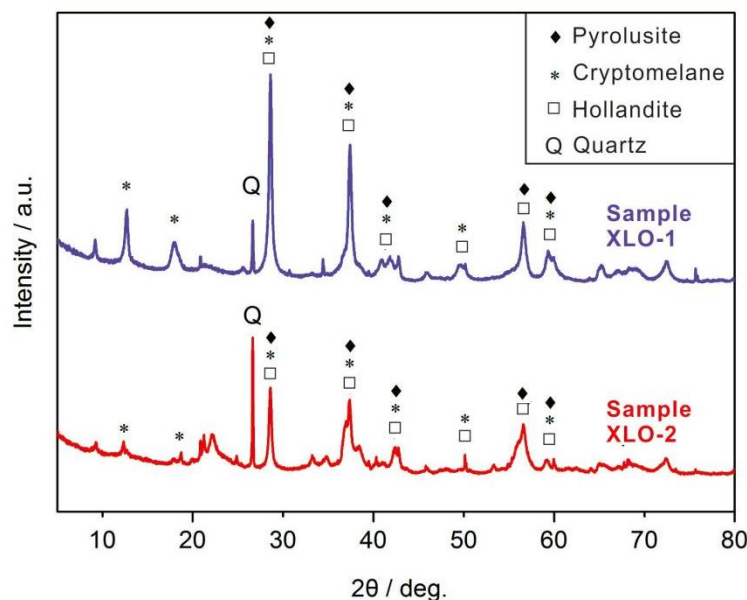


Figure 8. X-ray powder diffraction patterns of the Mn-oxide ore for samples XLO-1 and XLO-2.

5. Summary and Discussion

5.1. Mn Oxide Phases, Chemical Composition, and Genesis

In this study, petrography, bulk chemical composition, EPMA, and XRD were carried out to characterize the Mn oxide phases. The average Mn content of the Mn oxides determined in this study is 34.4 wt.% (Table 1), which is consistent with previous studies [12,19]. Pyrolusite, cryptomelane, and hollandite are the main Mn oxide ore minerals, and quartz is the primary gangue mineral.

The strong XRD peaks are consistent with cryptomelane and pyrolusite (Figure 8). Thus, in this case, depending solely on ideal chemical formula may not be sufficient for phase identification. Hollandite can be identified chemically as it contains Ba. In order to distinguish between pyrolusite and cryptomelane, optical microscopy and the K_2O mass fraction were applied.

Richmond and Fleischer [20] were the first to separate cryptomelane from a cryptocrystalline aggregate and demonstrated that cryptomelane is characterized by a high mass fraction of K_2O (3.10–3.88 wt.%). Detailed studies on the crystal structure of natural Mn-K ore (e.g., [2,21,22]) have resulted in the availability of a complete and detailed crystal structure data set. Gao et al. [23] studied the chemical composition of cryptomelane from the Xiangtan deposit (Hunan province, South China) with a K_2O mass fraction of 2.9–3.2 wt.%. Zhao et al. [14] studied the oolitic and pisolitic cryptomelane in the Xialei deposit and found that the K_2O was >2.5 wt.%. Vafeas et al. [24] studied fibrous cryptomelane from the todorokite-cryptomelane mineral assemblage at the Sebilo mine (northern Cape Province, South Africa) of which the cryptomelane K_2O is 4.4–7.0 wt.%. With regard to pyrolusite, the tunnels are too small to accommodate cations except for possibly H^+ . Consequently, most natural pyrolusite samples are close to the ideal composition [22], with a K_2O weight percent of 0.18–0.91 wt.% [25].

The Mn oxide ore can be classified into two types: (1) oolitic and pisolitic (often with annuli, Figures 3a–c and 4a,b), and (2) massive (Figures 3d–f and 4c–e). The EPMA results (Figure 7) show that the K_2O mass fraction in oolitic and pisolitic structure ranges from 2.31 to 4.33 wt.% (average of 3.60 wt.%), whereas the K_2O mass fraction in the massive structure varies between 0.03 and 2.21 wt.% (average of 0.53 wt.%). The oolitic and pisolitic Mn oxide shows a higher K_2O content than the massive Mn oxide. In the oolitic and pisolitic Mn oxide, the primary Mn oxide mineral is cryptomelane, confirming a previous study by Zhao et al. [14]. The massive Mn oxide, on the other hand, comprises dominantly pyrolusite with local cryptomelane (Figure 7). The pyrolusite-cryptomelane assemblage (Figure 4e) has been confirmed by EPMA. The cryptomelane is characterized by a K_2O mass fraction of 1.0–2.5 wt.%. Thus, the cryptomelane and pyrolusite are characterized by a $K_2O > 1$ and < 1 wt.%, respectively.

Pyrolusite is a stable MnO_2 phase in the supergene environment. When the potassium concentration in the formation environment is high, cryptomelane will replace pyrolusite [10,24,26]. The oolitic and pisolitic Mn oxide ore is pure cryptomelane, indicating a high degree of oxidation and a relatively high K mass fraction.

5.2. Crystal Structure of the Mn Oxide

Considerable attention has been paid to the tunnel structure in Mn oxides due to their excellent catalytic performances [27]. In pyrolusite, single chains of MnO_6 octahedra sharing corners with neighboring chains, build a framework structure containing tunnels (1×1), with the theoretical size of $\sim 0.23 \times 0.23 \text{ nm}^2$, forming a rutile-type structure. The crystal structure of cryptomelane and hollandite consists of two double edge-sharing MnO_6 octahedral chains forming a 2×2 tunnel, which are corner-connected to form one-dimensional tunnels, with a cryptomelane tunnel size of $\sim 0.46 \times 0.46 \text{ nm}^2$ [2,27].

Of the main Mn oxide ore minerals cryptomelane has been studied in detail by Lu and Li [11] and Zhao et al. [14]. Therefore, the crystal structure of pyrolusite and hollandite became the focus of our study. Hollandite shows far less information of crystal structure than pyrolusite because of its limited presence. In this study, the unit cell parameters for pyrolusite (tetragonal system) were refined, which is as follows for sample XLO-1: $a = 4.41 (\pm 0.01) \text{ \AA}$, $b = 4.41 (\pm 0.01) \text{ \AA}$, $c = 2.87 (\pm 0.01) \text{ \AA}$, $V = 55.96 (\pm 0.11) \text{ \AA}^3$, and for sample XLO-2: $a = 4.42 (\pm 0.01) \text{ \AA}$, $b = 4.42 (\pm 0.01) \text{ \AA}$, $c = 2.87 (\pm 0.01) \text{ \AA}$, $V = 56.01 (\pm 0.06) \text{ \AA}^3$. The size of the pyrolusite tunnels has been determined to be $2.6705 \times 2.6705 \text{ \AA}^2$ (Figure 9) using Diamond crystal modeling software.

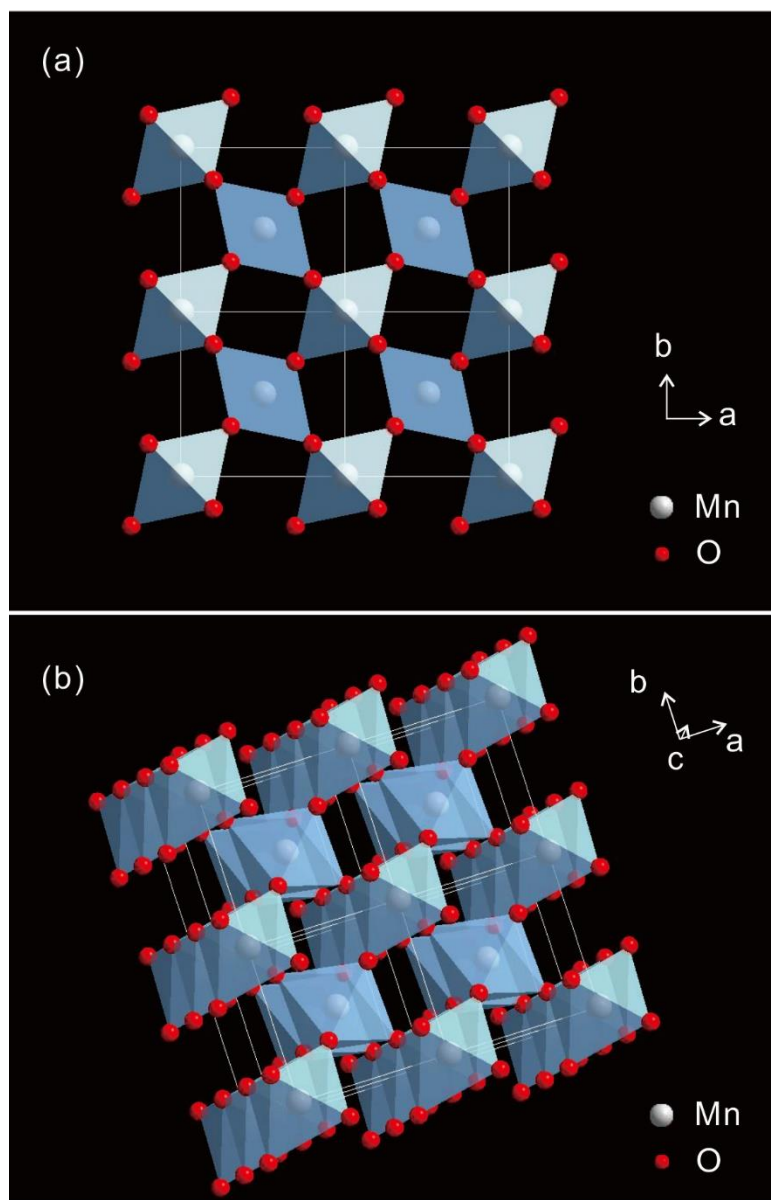


Figure 9. Crystal structure of pyrolusite (based on eight-unit cells) established by using the Diamond crystal modeling software. (a) The view perpendicular to c crystallographic axis; (b) the view skewed to c crystallographic axis.

Transition metal oxides (TMOs) are considered to be one of the most promising battery anode materials due to their high specific capacity, low cost, and wide practicability. Compared with other TMOs, Mn oxide has a lower conversion reaction potential, especially MnO (standard potential is 1.03 V); it is widely available, and it is environmentally friendly. It is a multi-electron reaction with great potential for anode material [28]. The synthetic material K-OMS-2 has been designed to manufacture high-energy-density batteries [29,30].

Mn oxide has wide applications in environmental purification techniques, in particular cryptomelane, which has a one-dimensional extended Mn oxide octahedral molecular sieve 2×2 pore structure (OMS-2) [10,14]. It can degrade phenolic organics in industrial wastewater [31,32] and decolorize printing and dyeing wastewater [33]. It also performs well in the absorption and decomposition of formaldehyde at room temperature [34]. Mn oxide can also affect organic matter cycling through adsorption, oxidative coupling, or oxidative decomposition (e.g., Mn oxide can degrade organic macromolecules in soil and water). In addition, Mn oxide can oxidatively couple small organic matter and participate

in the formation of humus, thereby reducing the bioavailability and toxicity of molecular organics [35,36].

6. Conclusions

The average Mn content of the Mn oxides in this study from the Xialei deposit in this study is 34.4 wt.%. The Mn oxide ore can be classified into two textural types: (1) oolitic and pisolitic Mn oxide, and (2) massive Mn oxide. Pyrolusite, cryptomelane, and hollandite are the main Mn oxide ore minerals in the supergene zone of the Xialei Mn deposit.

Scanning electron microscopy images show that the Mn oxide minerals in the Xialei deposit are present as fine-spherical with an earthy surface. TEM and HRTEM imaging show that the Mn oxides appear as oriented bundled and staggered nanorods, with nanopores between the crystal grains. The nanopore diameter ranges from a few nm to about 60 nm.

The cryptomelane and pyrolusite show notable different K₂O mass fractions. Only minor K₂O can enter the pyrolusite (K₂O a.f.p.u. < 0.2; K₂O wt.% < 1) because of the narrow space, whereas more K₂O can occur in the cryptomelane as a 2 × 2 tunnel cation (K₂O a.f.p.u. > 0.2; K₂O wt.% > 1).

The average refined unit cell parameters of pyrolusite (tetragonal system) are: a = 4.42 Å, b = 4.42 Å, c = 2.87 Å, V = 55.98 Å³. The pyrolusite tunnel size is 2.6705 × 2.6705 Å². The wide occurrence of pyrolusite and cryptomelane in the supergene zone of Xialei Mn deposit provides great potential for its usage in environmental mineralogy, electrodes, and molecular sieves.

Supplementary Materials: The following are available online at <https://www.mdpi.com/article/10.3390/min11111243/s1>, Table S1: EPMA results of the Mn oxide minerals in the Xialei deposit.

Author Contributions: S.N. prepared the manuscript; L.Z. provided the main idea and instructions on the design of the article; X.L. provide help on the conceptualization; T.C., Y.W. and L.M. supported the SEM, TEM and EPMA experiments; X.N. provided help on sample collection and supervised the manuscript preparation; H.W. and M.Z. investigate the geology of the Xialei deposit; J.M.H. reviewed and edited the manuscript; P.L. help to collected the samples and provide important documents on geology. All authors have read and agreed to the published version of the manuscript.

Funding: This research was funded by the Science and Technology Innovation Program of China Metallurgical Geology Bureau (grant No. CMGBK202106), Science and Technology Planning Project of Guangdong Province, China (grant No. 2020B1212060055), the Project of Institute of Mineral Resources Research, China Metallurgical Geology Bureau “A Preliminary Study on Environmental Mineralogy and Application of Low-grade Manganese Oxide Ore in Central Hunan-Western Guangxi”, and the National “Twelfth Five-Year” Plan for Science and Technology Support (grant No. 2011BAB04B10).

Data Availability Statement: Some data presented in this study are included within the article and supplementary materials. Other data are available on request from the corresponding author Liqun Zhao.

Acknowledgments: We are grateful to Zhenyu Chen for EPMA and to Lei Li for their support with SEM and TEM analysis. Many thanks are given to Lin Li and Guangyao Liu for their help with the XRD experiments. We thank colleagues from China Metallurgical Geology Bureau of Geological Prospecting Institute of Guangxi for their support during the sample collection.

Conflicts of Interest: The authors declare no conflict of interest.

References

1. Turekian, K.K.; Wedepohl, K.L. Distribution of the elements in some major units of the earth's crust. *Geol. Soc. Am. Bull.* **1961**, *72*, 175–192. [[CrossRef](#)]
2. Post, J.E. Manganese oxide minerals: Crystal structures and economic and environmental significance. *Proc. Natl. Acad. Sci. USA* **1999**, *96*, 3447–3454. [[CrossRef](#)] [[PubMed](#)]
3. Volokhin, Y.G.; Mikhailik, P.E.; Mikhailik, E.V. Minerals in manganese deposits of Belyaevsky Volcano, the Sea of Japan. *Russ. J. Pac. Geol.* **2020**, *14*, 340–362. [[CrossRef](#)]

4. Jin, S.S.; Zhang, L.M.; He, J.Z. Review of reactions of manganese oxides with organic compounds and applications of MnO_x in environmental remediation. *Acta Sci. Circumstantiae* **2008**, *28*, 2394–2403.
5. He, H.P.; Zhu, J.X.; Chen, M.; Tao, Q.; Tan, D.Y.; Liang, X.L.; Xian, H.Y. Progresses in researches on mineral structure and mineral physics (2011–2020). *Bull. Mineral. Petrol. Geochem.* **2020**, *39*, 697–713. (In Chinese with English Abstract)
6. Lu, A.H.; Li, Y.; Ding, H.R.; Wang, C.Q. “Mineral membrane” of the surface: “New sphere” of the Earth. *Acta Petrol. Sin.* **2019**, *35*, 119–128. (In Chinese with English Abstract)
7. Lu, A.H.; Li, Y.; Ding, H.R.; Wang, C.Q.; Xu, X.M.; Liu, F.F.; Liu, Y.W.; Zhu, Y.; Li, Y.Z. Natural mineral photoelectric effect: Non-classical mineral photosynthesis. *Earth Sci. Front.* **2020**, *27*, 179–194. (In Chinese with English Abstract)
8. Lu, A.H.; Li, Y.; Liu, F.F.; Liu, Y.W.; Ye, H.; Zhuang, Z.Y.; Li, Y.Z.; Ding, H.R.; Wang, C.Q. The photogeochemical cycle of Mn oxides on Earth’s surface. *Mineral. Mag.* **2021**, *85*, 1–57. [[CrossRef](#)]
9. Zhang, C.M.; Pang, X.; Wang, Y.Z. Controllable synthesis of one-dimensional cryptomelane-type manganese dioxide and its electrochemical performance. *Acta Chim. Sin.* **2018**, *76*, 133–137. (In Chinese with English Abstract) [[CrossRef](#)]
10. Lu, A.H.; Gao, X.; Qin, S.; Wang, C.Q. Cryptomelane (K_xMn_{8-x}O₁₆): Natural active octahedral molecular sieve (OMS-2). *Chin. Sci. Bull.* **2003**, *6*, 97–100. (In Chinese with English Abstract)
11. Lu, A.H.; Li, Y. Reactivity of natural Mn oxide cryptomelane. In *Advances in the Environmental Biogeochemistry of Manganese Oxides*; ACS Symposium Series; ACS Publications: Washington, DC, USA, 2015; pp. 89–106.
12. Zeng, Y.Y.; Liu, T.B. Characteristics of the Devonian Xialei manganese deposit, Guangxi Zhuang Autonomous Region, China. *Ore Geol. Rev.* **1999**, *15*, 153–163. [[CrossRef](#)]
13. Zhu, J.D.; Zhu, K.J.; Zhou, S.G.; Tian, Y.M.; Zhang, Z.W.; Li, S.F.; Shi, C.H. Characteristics and genesis of deposits in the Xialei-Dongping Manganese Ore Belt of Guangxi Province. *Geol. Explor.* **2016**, *52*, 846–853. (In Chinese with English Abstract)
14. Zhao, D.J.; Lu, A.H.; Wang, L.J.; Zheng, X.K.; Liu, R.; Guo, Y.J. Mineralogical characteristics study of natural cryptomelane in the Xialei Manganese Deposit, Guangxi. *Acta Sci. Nat. Univ. Pekin.* **2005**, *41*, 859–868. (In Chinese with English Abstract)
15. Ismail, S.; Hushim, S.F.S.; Hussin, H.; Abdullah, N.S. Chemical and mineralogical characterization of Malaysian low-grade manganese ore. *Period. Mineral.* **2016**, *85*, 277–288.
16. Wang, H.Z.; Shi, X.Y.; Wang, X.X. *Research on Sequence Stratigraphy in China*; Guangdong Science and Technology Press: Guangzhou, China, 2000; pp. 1–457.
17. Zhao, L.Q.; Zhou, S.G.; Yi, H.S.; Dong, S.Y.; Li, L.M.; Zhang, M. Geochemical characteristics and sedimentary environment of the Xialei manganese deposit in southwest Guangxi. *Geol. Explor.* **2016**, *52*, 25–39. (In Chinese with English Abstract)
18. Yan, D.R.; Li, J.W.; Hu, M.A.; Lang, Y.S. Characteristics and genesis of supergene manganese ores in Xialei, Guangxi. *Geol. Sci. Technol. Inf.* **2006**, *25*, 61–67. (In Chinese with English Abstract)
19. Hao, R.X.; Guan, G.Y. The mineral assemblages and oxidizing mechanism of oxidized manganese deposits of Xialei-Hurun manganese mineralized zone. *China’s Manganese Ind.* **1995**, *13*, 3–7. (In Chinese with English Abstract)
20. Richmond, W.E.; Fleischer, M. Cryptomelane, a new name for the commonest of the “psilomelane” minerals. *Am. Mineral.* **1942**, *27*, 607–610.
21. Post, J.E.; Dreele, R.B.V.; Buseck, P.R. Symmetry and cation displacements in hollandites: Structure refinements of hollandite, cryptomelane and priderite. *Acta Crystallogr.* **1982**, *38*, 1056–1065. [[CrossRef](#)]
22. Post, J.E.; Mckeown, D.A.; Heaney, P.J. Raman spectroscopy study of manganese oxides: Tunnel structures. *Am. Mineral.* **2020**, *105*, 1175–1190. [[CrossRef](#)]
23. Gao, X.; Lu, A.H.; Qin, S.; Zheng, D.S.; Zheng, X.K.; Zheng, Z. A study of crystal structural characteristics and environmental properties of natural cryptomelane. *Acta Petrol. Mineral.* **2001**, *20*, 477–484.
24. Vafeas, N.A.; Viljoen, K.S.; Blygnaut, L.C. Characterization of fibrous cryptomelane from the todorokite-cryptomelane mineral assemblage at the Sebilo Mine, Northern Cape Province, South Africa. *Can. Mineral.* **2018**, *56*, 65–76. [[CrossRef](#)]
25. Wang, P.; Pan, Z.L.; Weng, L.B. *Systematic Mineralogy*; Geological Publishing House: Beijing, China, 1987; pp. 1–654. (In Chinese)
26. Bricker, O.P. Some stability relations in the system Mn-O₂-H₂O at 25 °C and one atmosphere total pressure. *Amer. Mineral.* **1965**, *50*, 1296–1354.
27. Chen, T.; Dou, H.Y.; Li, X.L.; Tang, X.F.; Li, J.H.; Hao, J.M. Tunnel structure effect of manganese oxides in complete oxidation of formaldehyde. *Microporous Mesoporous Mater.* **2009**, *122*, 270–274. [[CrossRef](#)]
28. Galezowski, L.; Recham, N.; Larcher, D.; Miot, J.; Skouri-Panet, F.; Guyot, F. Microbially induced mineralization of layered Mn oxides electroactive in Li batteries. *Front. Microbiol.* **2020**, *11*, 2031. [[CrossRef](#)]
29. Poyraz, A.S.; Huang, J.P.; Wu, L.J.; Bock, D.C.; Zhu, Y.M.; Marschilok, A.C.; Takeuchi, K.J.; Takeuchi, E.S. Potassium-based alpha-manganese dioxide nanofiber binderfree self-supporting electrodes: A design strategy for high energy density batteries. *Energy Technol.* **2016**, *4*, 1–12. [[CrossRef](#)]
30. Zhang, Q.; Didier, C.; Pang, W.K.; Liu, Y.J.; Wang, Z.J.; Li, S.; Peterson, V.K.; Mao, J.F.; Guo, Z.P. Structural insight into layer gliding and lattice distortion in layered manganese oxide electrodes for potassium-ion batteries. *Adv. Energy Mater.* **2019**, *9*, 1900568. [[CrossRef](#)]
31. Li, G.Y.; Lu, A.H.; Gao, X.; Zhao, Y.Q.; Li, Q.R.; Yang, X. An investigation into the oxidation and degradation of phenol in water by natural cryptomelane. *Acta Petrol. Mineral.* **2003**, *22*, 162–166. (In Chinese with English Abstract)
32. Li, G.Y.; Lu, A.H.; Rao, Z. Mechanism of oxidation and degradation of phenol in water by natural cryptomelane. *Acta Petrol. Mineral.* **2003**, *22*, 365–368. (In Chinese with English Abstract)

33. Yang, X.; Lu, A.H.; Li, G.Y.; Li, Q.R.; Gao, X.; Ren, Z.P. Oxidative decolorization of printing and dyeing wastewater by natural cryptomelane. *Acta Petrol. Mineral.* **2003**, *22*, 370–373. (In Chinese with English Abstract)
34. Zhao, L.Q.; Niu, S.D.; Li, L.; Niu, X.L.; Wu, H.Y.; Mo, L.C.; Chen, T.; Zhang, M. Mineralogy and crystal structure studies of the manganese oxide in Xiangtan manganese deposit, South China and its preliminary application on absorption and catalysis of formaldehyde. In Proceedings of the Goldschmidt Conference, Lyon, France, 4–9 July 2021.
35. Jokic, A.; Frenkel, A.I.; Vairavamurthy, M.A.; Huang, P.M. Birnessite catalysis of the maillard reaction: Its significance in natural humification. *Geophys. Res. Lett.* **2001**, *28*, 3899–3902. [[CrossRef](#)]
36. Selig, H.; Keinath, T.M.; Weber, W.J. Sorption and manganese-induced oxidative coupling of hydroxylated aromatic compounds by natural geosorbents. *Environ. Sci. Technol.* **2003**, *37*, 4122–4127. [[CrossRef](#)] [[PubMed](#)]